Nonlocal interaction engineering of 2D roton-like dispersion relations in acoustic and mechanical metamaterials

Ke Wang[1,2]†, Yi Chen[1]†*, Muamer Kadic[1,3], Changguo Wang[2], Martin Wegener[1,4]

[1]Institute of Applied Physics, Karlsruhe Institute of Technology (KIT), Karlsruhe 76128, Germany.

[2]Center for Composite Materials, Harbin Institute of Technology, Harbin 150001, P.R. China.

[3]Institut FEMTO-ST, UMR 6174, CNRS, Université de Bourgogne Franche-Comté, Besançon 25030, France.

[4]Institute of Nanotechnology, Karlsruhe Institute of Technology (KIT), Karlsruhe 76128, Germany.

*Correspondence to: yi.chen@partner.kit.edu

†These authors contributed equally.

Abstract

The interior of the synthetic unit cells and their interactions determine the wave properties of metamaterials composed of periodic lattices of these cells. While local interactions with the nearest neighbors are well appreciated, nonlocal beyond-nearest-neighbor interactions are often considered as a nuisance. Here, by introducing a versatile effectively two-dimensional metamaterial platform for airborne sound and elastic waves, we exploit nonlocal effects as a powerful design tool. Within a simplified discrete model, we analytically show that the lowest band can be engineered by Fourier synthesis, where the N-th order Fourier coefficient is determined by the N-th nearest-neighbor interaction strength. Roton-like dispersion relations are an example. The results of the discrete model agree well with a refined model and with numerical calculations. In addition, we engineer the passage of waves from a local metamaterial into a nonlocal metamaterial by carefully tailoring the transition region between the two.

Keywords: beyond-nearest-neighbor interactions, nonlocality, metamaterials, phonons, acoustic waves, elastic waves, roton

Introduction

In the solid-state physics of ordinary crystals, interactions way beyond the nearest atomic neighbors can be of crucial importance, for example for the crystal's ionic binding energy [1]. The Madelung constant [2] summarizes the effects of this long-range Coulomb interaction. In electromagnetism and optics, for artificial crystals called metamaterials [3, 4], long-range interactions are well known to play an important role as well [5, 6]. For example, the dynamic electric dipole-dipole interaction asymptotically decays inversely with the distance between dipoles just like the static Coulomb potential [1, 7]. So far, however, long-range interactions in electromagnetic or optical metamaterials have mainly been considered as a nuisance that complicates the physics rather than as a useful design feature [5].

In contrast, when conceptually introducing acoustical and optical phonons in ordinary crystals by mass-and-spring type models [1], the Hooke's springs emerging from a given mass are usually only connected to the immediate neighbors of this mass [8-11]. In few cases, springs between next-nearest neighbors have been considered as a correction [12, 13]. For many years, this only-nearest-neighbor spirit has also been taken for designing phonon dispersion relations in mechanical or acoustical metamaterials [3, 10, 14-17]. Few exceptions have discussed the influence of long-range interactions in linear elastic materials [18-20] or in phononic crystals [21-23], albeit not in the spirit of a design tool but again rather as a correction to ordinary behavior.

Recently, we showed that suitable metamaterial designs using sufficiently strong N-th nearest-neighbor interactions with $N = 3$, in addition to the usual nearest-neighbors interactions ($N = 1$), allow for obtaining unusual acoustical-wave dispersion relations [24, 25], which mimic the famous rotons in superfluid helium [26-29]. However, the three-dimensional (3D) architectures discussed therein [24, 25, 30] were restricted in three regards, i)-iii). i) They were limited to tailoring the dispersion relation along only a single propagation direction. ii) They were not flexible enough to provide interactions way beyond $N = 3$. iii) They could not easily be generalized to support more than just two types of interactions (nearest-neighbor and third-nearest-neighbor) simultaneously.

We note in passing that another recent publication [31] used beyond-nearest-neighbor interactions in mechanical metamaterials to design and tailor the properties of higher phonon bands and states with the aim of obtaining topological band gaps. This work is not of immediate importance here because we focus on the lowest acoustical band.

Herein, we introduce and analyze by numerical and analytical calculations a flexible effectively two-dimensional metamaterial platform that allows for tailoring the lowest acoustical phonon dispersion relation for airborne sound by using beyond-nearest-neighbor interactions along two orthogonal directions. We design the long-range interactions by a network of cylindrical tubes, which connect cuboid compartments in a two-dimensional square array. The numerically calculated phonon bands reveal multiple roton-like minima along multiple directions. Through a simplified discrete analytical model for the lowest (acoustical) band that is mathematically equivalent to a mass-and-spring model, we show that the long-range interactions directly determine the Fourier coefficients of the acoustical-wave dispersion relation. Based on the simple model, we further demonstrate interesting negative refraction [32, 33] and triple refraction at an interface between two metamaterials with and without beyond-nearest-neighbor interactions, respectively. We emphasize the importance of the transition region between an ordinary medium and the metamaterial comprising beyond-nearest-neighbor interactions as to which mode in the metamaterial the incident wave couples to. These calculations highlight the aspect of nonlocality [20, 31], which is due to the beyond-nearest-neighbor interactions. We also propose a refined analytical model that can capture the higher bands in the band structure as well. The combination of these aspects shows that nonlocal effects are a powerful tool for designing acoustic and elastic metamaterials.

Results and Discussion

Metamaterial design and numerical calculations. To implement the Fourier-synthesis idea in the simplest possible yet practical way, we consider airborne acoustical sound. Here, only longitudinally polarized pressure waves occur [34]. We consider the air in tubes with rigid walls as mediator of the interactions. In acoustics, such hollow tubes do not lead to a finite minimum ("cut-off") frequency, below which propagating waves do not occur. The behavior of airborne waves can easily be transferred to waterborne acoustical waves. In contrast, for waves in general elastic structures, two transverse modes occur in addition to the longitudinal modes. The situation would also be more complex for transversely polarized electromagnetic waves, for which tubes with walls made of a perfect electrical conductor do lead to a finite cut-off frequency [35]. Such finite-frequency cut-off obviously inhibits an "acoustical" mode starting from zero frequency at zero wavenumber.

Figure 1(a) shows one unit cell of the suggested 3D structure of the metamaterial for airborne sound for the example of $N = 3$. Panel (b) illustrates the resulting two-dimensional lattice. Panel (c) shows the unit

cell for the fix cases $N = 4, 5, 6, 7, 8$. In all of these cases, we consider a two-dimensional square lattice of hollow compartments with lattice constant a. The walls of these compartments are treated as rigid bodies. Mathematically, this corresponds to Neumann boundary conditions for the pressure field [34]. Intuitively, the compartments can be seen as the "atoms". Tubes connecting the compartments can be seen as mediators of the interactions among the atoms. Four thin tubes with inner radius r_1 directly connect each of these compartments with its four immediate neighbors. The walls of all tubes are treated as Neumann boundaries, too. These tubes mediate the nearest-neighbor interactions between the compartments. The thicker tubes with inner radius $r_N > r_1$ mediate the beyond-nearest-neighbor interactions with $N \geq 2$. To avoid collision of the tubes along the x- and the y-direction, respectively, one set of tubes is located above the xy-plane spanned by the thin tubes and the other one below. Therefore, the metamaterial structure itself has only two-fold rotational symmetry with respect to the z-axis. However, the structure exhibits an additional rotation-reflection symmetry with respect to the xy-plane. This symmetry ensures that the phonon dispersion relation $\omega_n(k_x, k_y)$, which connects the angular frequency ω_n of the band with band index n and wave vector $\mathbf{k} = (k_x, k_y)$, has four-fold rotational symmetry, i.e., wave propagation along the x- and y-direction are strictly equivalent by symmetry. For a given fixed radius of the tubes, the maximum possible integer N is clearly limited by geometrical constrains (cf. Fig. 1(c)). For the radii chosen in Fig. 1, the maximum possible value is $N = 8$ as the tubes would overlap for $N = 9$. However, conceptually, one can consider the limit of $r_1 \to 0$ at fixed finite ratio r_N/r_1. In this limit, integers up to $N \to \infty$ are possible mathematically.

So far, we have only considered structures supporting nearest-neighbor interactions and N-th nearest-neighbor interactions with a single specific value of N. However, the metamaterial platform in Fig. 1(b) can easily be generalized to support several different beyond-nearest-neighbor interactions simultaneously. Figure 2 shows as an example a metamaterial structure supporting the three interactions with $N = 1$, $N = 3$, and $N = 5$. The $N = 3$ interactions lie in planes parallel to the xy-plane at different z-positions than the $N = 5$ interactions. Clearly, for the chosen metamaterial platform, any further values of N can be realized at yet different z-positions without imposing any geometrical constrains or difficulty (not depicted).

To compute the phonon dispersion relation of airborne acoustical waves propagating in the channel system shown in Figs. 1-2, we consider the scalar wave equation for the spatial air-pressure modulation $\tilde{P}_{\mathbf{k},i}(\mathbf{r})$ on top of a constant background air pressure $P_0 \gg \tilde{P}_{\mathbf{k},i}(\mathbf{r})$ at spatial position $\mathbf{r} = (x, y, z)$ and two-dimensional wave vector $\mathbf{k} = (k_x, k_y)$ [1]. We neglect damping. This assumption is expected to be

reasonable if all absolute dimensions are sufficiently large [36]. Furthermore, we have also performed calculations including damping (see Supplementary Note 1). The relative differences of the (real part of the) eigenfrequencies with respect to the lossless case are smaller than 4% for all cases (cf. Figure 3 and Supplementary Figures 1 and 2). The qualitative behavior is not changed at all. In the Fourier-domain, the resulting eigenvalue problem [34] reads

$$\mathbf{\nabla} \cdot \left(\mathbf{\nabla} \tilde{P}_{\mathbf{k},n}(\mathbf{r}) \right) = -\frac{\omega_n^2(\mathbf{k})}{v_{\mathrm{air}}^2} \tilde{P}_{\mathbf{k},n}(\mathbf{r}).$$

The band with index $n = 1$ corresponds to an acoustical branch, the bands with $n \geq 2$ can be seen as "optical" phonon bands. We will focus our below design and discussion on the lowest band with $n = 1$, but we will graphically also show several higher-frequency bands for completeness. We choose $v_{\mathrm{air}} = 343 \ \mathrm{m/s}$ as the constant speed of sound in air. We solve this eigenvalue equation by a finite-element method (FEM) implemented in the commercial software Comsol Multiphysics. We assume Bloch periodic boundary conditions along the x- and the y-direction and treat the walls of all compartments and tubes as rigid immovable bodies via Neumann boundary conditions [35]. All geometrical parameters of the metamaterial architecture are defined and given in Figs. 1-2. As usual, the first 2D Brillouin zone of the 2D square lattice is given by the conditions $|k_x| \leq \pi/a$ and $|k_y| \leq \pi/a$.

Examples of calculated band structures are given in Figs. 3-5. Figure 3 shows the band structure of the metamaterial depicted in Fig. 1. It contains beyond-nearest-neighbor interactions with $N = 3$. These 2D band structures can be compared with our previous quasi-1D band structures [24]. Figure 3(a) shows the angular frequency for the usual tour through the 2D Brillouin zone (also see inset). Figure 3(b) represents the same results in 2D $\mathbf{k}$-space. It can be seen that we obtain local minima of the dispersion relation of the lowest acoustic band along the $(k_x, 0)$ direction and the equivalent $(0, k_y)$ direction. These local minima resemble the roton-like dispersion relations discussed in detail previously [24]. In addition, we find four further (roton-like) local minima along the diagonals. As expected from the symmetry of the metamaterial structure (see above), the dispersion relation $\omega_1(k_x, k_y)$ exhibits four-fold rotational symmetry. However, it is clearly not isotropic. The depth of the minima can be tailored by the effective strength of the beyond-nearest-neighbor interaction compared to the nearest-neighbor interactions, i.e., by the ratio of the tube radii r_3/r_1 (not depicted). The minimum is absent for $r_3/r_1 > 0$, becomes deeper for increasing ratio $r_3/r_1 = 0$, and touches zero angular frequency, $\omega_1 = 0$, in the limit of $r_3/r_1 \to \infty$.

Figure 4 shows the same as Fig. 3(a), but for different values of N instead of $N = 3$. These results correspond to the metamaterial unit cells shown in Fig. 1. We find that the number of oscillations versus wave number within the first Brillouin zone increases with increasing N. This behavior already suggests a connection between the integer N and the corresponding Fourier component. We will come back to this aspect in more detail in the following section.

Figure 5 is as Fig. 4 (where $N = 3$ only), but for two different orders of long-range interaction in parallel, namely (a) $N = 4$ in addition to $N = 3$, (b) $N = 5$ in addition to $N = 3$, and (c) $N = 6$ in addition to $N = 3$. The corresponding metamaterial unit cells have already been shown in Fig. 2. Again, the angular frequency of the lowest acoustical band exhibits an oscillatory behavior versus wave number $\mathbf{k}$, however, now with two different Fourier components superimposed. We will come back to this aspect in more detail in the following section.

Mass-and-spring model. To obtain a more intuitive as well as an approximate analytical understanding for the findings of the previous section, we now consider a simple discrete analytical model. This model shows that the acoustical dispersion relation of the metamaterial structures shown in Figs. 1-2 can be tailored in the sense of Fourier synthesis. The beyond-nearest-neighbor interactions determine the Fourier coefficients.

We consider the mass-and-spring model shown in Fig. 6. We show that Newton's equation of motion for the masses in this 2D lattice is mathematically equivalent to the approximate equation of motion for the air mass in the cuboid compartments shown in yellow in Fig. 1(b). The hollow tubes connecting these compartments correspond to Hooke's springs. This ansatz follows our previous reasoning [24, 25] and is consistent with the numerically calculated air-pressure fields. An example referring to the parameters used in Figure 3 is depicted in Supplementary Figure 3. We emphasize that this simple model accounts for the lowest (acoustical) band with $n = 1$ only, as the model contains only one degree of freedom (the position of the single mass in the unit cell). We will expand the analytical modelling to also include the higher bands with $n \geq 2$ in the following section. Let us now derive the discrete model with a discrete set of equations of motion for the metamaterial structures illustrated in Figs. 1-2.

Within the cuboid air compartment with volume V_c at the 2D lattice site defined by the pair of integers (m, n), the air pressure $P_{mn} = P_0 + \tilde{P}_{mn}$ shall be approximated by the constant mean pressure in that compartment. The air pressure directly translates into the number of air molecules $N_{mn} = N_0 + \tilde{N}_{mn}$ in

one compartment. N_0 is the number of air molecules in the compartment at fixed room temperature T, corresponding to the background pressure P_0. The ideal-gas equation becomes $P_{mn} = N_{mn}k_{\mathrm{B}}T/V_{\mathrm{c}}$ or $\tilde{P}_{mn} = \tilde{N}_{mn}k_{\mathrm{B}}T/V_{\mathrm{c}}$, with the Boltzmann constant k_{B}. Furthermore, in each Nth-nearest-neighbor horizontal and vertical tube with radius r_N (see above), hence cross section πr_N^2, and length L_N, we approximate the air velocity along the tube axis as being constant throughout that tube. We define the corresponding velocities in the horizontal (x-direction) tubes, $h_{mn}^{(N)}$, and those in the vertical (y-direction) tubes, $v_{ij}^{(N)}$, mediating the N-th order interaction. The mass density, ρ_0, within all tubes is approximated as being constant, with $\rho_0 = m_0 P_0/(k_{\mathrm{B}}T)$, where m_0 is the mass of one air molecule. With these definitions, the continuity equation applied to compartment (m, n) describes the in- and out-flux of air molecules from the tubes into the compartment and reads

$$\frac{\mathrm{d}}{\mathrm{d}t}m_0 N_{mn} = \frac{\mathrm{d}}{\mathrm{d}t}m_0\tilde{N}_{mn} = \sum_{N=1}^{\infty} -\rho_0\pi r_N^2\left(\left(h_{mn}^{(N)} - h_{m-N,n}^{(N)}\right) + \left(v_{mn}^{(N)} - v_{m,n-N}^{(N)}\right)\right). \tag{1}$$

The acceleration $\frac{\mathrm{d}}{\mathrm{d}t}h_{mn}^{(N)}$ in the Nth-order horizontal tubes results from the net force corresponding to the pressure difference between the two ends of the tube with length L_N, i.e., from

$$\rho_0\frac{\mathrm{d}}{\mathrm{d}t}h_{mn}^{(N)} = -\frac{\tilde{P}_{m+N,n} - \tilde{P}_{mn}}{L_N}, \tag{2}$$

and likewise for the Nth-order vertical tubes

$$\rho_0\frac{\mathrm{d}}{\mathrm{d}t}v_{mn}^{(N)} = -\frac{\tilde{P}_{m,n+N} - \tilde{P}_{mn}}{L_N}. \tag{3}$$

Taking the time derivative of Eq. (1), inserting Eqs. (2) and (3) into Eq. (1), and replacing $\tilde{N}_{mn} = \frac{\rho_0 V_{\mathrm{c}}}{MP_0}\tilde{P}_{mn}$ leads to

$$M\frac{\mathrm{d}^2}{\mathrm{d}t^2}\tilde{P}_{mn} = \sum_{N=1}^{\infty} K_N\left(\left(\tilde{P}_{m-N,n} - 2\tilde{P}_{mn} + \tilde{P}_{m+N,n}\right) + \left(\tilde{P}_{m,n-N} - 2\tilde{P}_{mn} + \tilde{P}_{m,n+N}\right)\right), \tag{4}$$

where we have introduced the two abbreviations

$$M = \rho_0 V_{\mathrm{c}} \tag{5}$$

and

$$K_N = P_0\frac{\pi r_N^2}{L_N}. \tag{6}$$

Equation (4) is identical to Newton's equation for the mass-and-spring model shown in Fig. 6 if the pressure variation $\tilde{P}_{m,n}$ in Eq. (4) is replaced by the out-of-plane displacement. M in Eq. (4) is the air mass in one compartment. It is the same for all lattice sites at this point. Below, when addressing interfaces, we will consider different values of M at different locations. According to Eq. (5), the mass M can be varied in practice by changing the volume of the compartment V_c. K_N is the effective Hooke's spring constant for the Nth order interaction. According to Eq. (6), it can be tailored by the radius of the Nth order tube, r_N. Obviously, at fixed tube radius r_N, the effective spring constant K_N decreases inversely versus increasing order N of the interaction, hence with increasing length $L_N \approx N L_1$ of the tube for $N \geq 2$. This behavior is perfectly analogous to that of an ordinary elastic Hooke's spring. As the tube diameter $2r_N$ is geometrically constrained in size from above (cf. Fig. 1), and must eventually decrease with increasing N, the effective relative strength of the Nth-order interaction eventually tends to zero inversely proportional to the order N, or stronger than that. In the previous section, we have seen that values up to $N = 8$ can be achieved in practice.

Making a plane-wave ansatz for Eq. (4) according to

$$\tilde{P}_{mn} = \tilde{P} \exp\big(\mathrm{i}(m k_x a + n k_y a - \omega t)\big), \tag{7}$$

with constant amplitude prefactor $\tilde{P}$, we obtain the dispersion relation for acoustical pressure waves with band index $n = 1$ in the discrete model

$$\omega_1^2\big(k_x, k_y\big) = \sum_{N=0}^{\infty} F_N \cos(N k_x a) + \sum_{N=0}^{\infty} F_N \cos\big(N k_y a\big). \tag{8}$$

This expression is central to our paper. We see that, for $N \geq 1$, the Fourier coefficient F_N in the two Fourier series on the right-hand side is directly connected to the Nth nearest-neighbor effective Hooke's spring constant K_N and is given by

$$F_N = -2 K_N / M. \tag{9}$$

The constant 0th-order term of the Fourier series with

$$F_0 = \sum_{N'=1}^{\infty} 2 K_{N'} / M \tag{10}$$

guarantees that the dispersion relation Eq. (7) starts according to

$$\omega_1(k_x, k_y) \propto |\mathbf{k}| \tag{11}$$

in the limit $|\mathbf{k}| \rightarrow 0$. This is equivalent to saying that we restrict ourselves to "acoustical" dispersion relations. In the Fourier series on the right-hand side of Eq. (8), only cosine terms appear as sine terms would generally violate the reciprocity condition $\omega(-\mathbf{k}) = \omega(\mathbf{k})$.

For suitable parameters, the above simple 2D discrete model again exhibits roton-like dispersion relations along multiple directions (see Supplementary Note 2 and Supplementary Figure 4). To allow for a direct comparison with the above numerical calculations, we plot the calculated dispersion relations of this model (red dots) together with those of the numerical calculations (gray curves) in Fig. 3 and Fig. 4. For the lowest band, the overall agreement is excellent for all values of N. This especially holds true for the principal direction $\mathbf{\Gamma M}$. Quantitative discrepancies occur for other directions, but the agreement is still qualitatively good. Note, however, that we have taken the freedom to use fitted ratios K_N/M. In principle, these ratios could be calculated from Eqs. (5) and (6) and from the known geometrical parameters therein. The fitting procedure gives us freedom to correct for the simplicity of the mass-and-spring model. We will come back to a more stringent treatment in the following section.

Before we get there, we now apply the mass-and-spring model to treating metamaterials that are not infinitely extended, but that rather contain interfaces. The treatment of such configurations would be computationally very expensive on the level of the complete numerical calculations.

As a representative example, we consider only nearest-neighbor interactions and third-nearest-neighbor interactions ($N = 3$). In such a system [24], the dispersion relation does not monotonically increase but features a region of backward waves, with negative scalar product of the phase and group velocity vectors, and a roton-like [26, 28] local minimum in the dispersion relation. We expect interesting wave behavior, including negative refraction and triple refraction, which we shall study in the remainder of this section.

The considered interface and excitation configuration is illustrated in Fig. 7. In the region above the interface, we consider a discrete system simultaneously with nearest-neighbor interactions and third-nearest-neighbor interactions ($N = 3$). In the region below the interface, we assume only nearest-neighbor interactions. We force displacements of masses located on the indicated black line according to $\cos(2\pi f_c t)\exp(-(\pi f_c t/50)^2)\exp(-((x-x_c)^2 + (y-y_c)^2)/37.5^2)$, with $x_c = -100$, $y_c = -130$ being the coordinate of the middle point of the line in units of the lattice constant a, and f_c being the carrier frequency of the temporally Gaussian excitation signal. This excitation launches a spatially Gaussian wave packet towards the interface at an oblique angle of 45°. We have chosen this particular angle just as an example to illustrate the principle. The temporal Gaussian envelope contains about 50

oscillation cycles (see Fig. 7(c)), corresponding to a fairly narrow spread in the frequency domain (see Fig. 7(d)).

Due to the mismatch of interaction orders between the two regions at the interface, one of the Hooke's springs that mediate the third-nearest-neighbor interactions for the first three masses above the interface (see Fig. 7(b)) is truncated by the interface. Therefore, the connections at the interface are modified slightly (see Fig. 7(b)). These modifications in the transition region between the two media will turn out to be crucial for controlling the transmitted and reflected partial waves. As shown in the below simulations, which are based on a trial-and error procedure for the design and for the parameters of the transition layer, we can even achieve nearly 100% transmission for each of the three possible modes individually by fine-tuning the indicated interface parameters, including the two mass parameters, M_{01} and M_{02}, and three spring constants, K_{01}, K_{02} and K_{03} in Fig. 7. Alternatively, the parameters for the transition region can be chosen such that an incident wave couples to all three refracted modes simultaneously (see Supplementary Figure 7).

We note in passing that an explicit and rational construction procedure for the transition layer between a local and a non-local medium and its parameters is presently elusive to our knowledge. Defining such a procedure beyond a trial-and-error approach is beyond the scope of our present paper.

In Figure 8, we first demonstrate negative refraction at the interface. For the incidence region, we choose the parameters $M/M_0 = 1.0, K_1/K_0 = 1.2$, and $K_3/K_0 = 0$. Here, M_0 and K_0 are not relevant to the results and can take any constant reference values. In Fig. 8(a), red (blue) solids lines represent iso-frequency contours for the discrete system in the incidence (transmission) region at carrier frequency (= center frequency) $\omega/\omega_0 = 0.7$ of the Gaussian wave packed used in the numerical simulation. Dashed lines correspond to a slightly larger frequency. From two nearby iso-frequency contours, we can identify the group velocity vector $\mathbf{v}_g$. From Snell's law, one negatively refracted mode with wave vector $\mathbf{k}_t$ and group velocity $\mathbf{v}_g$ is expected. A snapshot of the simulated displacement fields at one instant in time, $t/T_c = 150$, is shown in Fig. 8(b). The interface parameters, as indicated in the figure, are tuned to achieve a nearly zero reflected partial wave. As expected, the refracted waves exactly move along the direction of the predicted group velocity $\mathbf{v}_g$. The phase fronts of the refracted waves move along the wave vector $\mathbf{k}_t$. The dashed lines are guides to the eye for the wave propagation trajectory. The negative refraction can be seen yet more clearly in the Supplementary Movie 1.

Next, we demonstrate triple refraction. In this case, we choose different parameters for the incidence region, namely $M/M_0 = 0.44, K_1/K_0 = 2.3$, and $K_3/K_0 = 0$. The carrier frequency of the Gaussian packet is chosen as $\omega_c/\omega_0 = 0.9$. Iso-frequency contours are depicted in Fig. 9 the same manner as in Fig. 8(a). For this case, there are three possible refracted modes, with the wave vectors and the group velocities, $\mathbf{k}_{t1}$ and $\mathbf{v}_{g1}$, $\mathbf{k}_{t2}$ and $\mathbf{v}_{g2}$, and $\mathbf{k}_{t3}$ and $\mathbf{v}_{g3}$, respectively, instead of a single mode as in the previous example. The third mode is again a backward wave with $\mathbf{k}_{t3} \cdot \mathbf{v}_{g3} < 0$. The importance of the interface parameters becomes evident from the three different calculations shown in Fig. 10(a)-(c). In each of the three cases, one of the three different modes is excited almost exclusively. This means that one can select a wanted mode by appropriately choosing the parameters of the transition region between the two media. For all three cases, we further illustrate the behavior by the Supplementary Movies 2-4.

We note in passing that the rich physics of the transition region can likely also be captured by generalizing the effective-medium approximation of the mass-and-spring model in terms of a generalized wave equation for homogeneous non-local media, as introduced in [25], to the case of heterogeneous non-local elastic media. However, this aspect goes well beyond the scope of the present paper.

Refined analytical model. In this section, we present a refined analytical model, which captures not only the behavior of the lowest band but also that of the higher bands for the proposed metamaterials. We make the following two assumptions: i) The acoustic pressure in the cuboid compartments in Fig. 1 is approximated as being constant within. ii) The pressure modes in all tubes are the fundamental waveguide mode, i.e., at a given position along the tubes, the pressure is constant over the cross section [34]. These two assumptions are expected to be valid for low-frequency sound, for which the wavelength in air is much larger than the unit cell size.

On this basis, we derive the metamaterial dispersion relations analytically based on the Floquet-Bloch theorem [1]. As an ansatz, the acoustic pressure modulation at the lattice site defined by the pair of integers (m, n) is given by $\tilde{P}_{mn} = \tilde{P} \exp\left(i(k_x ma + k_y na - \omega t)\right)$, with $\tilde{P}$ being a constant prefactor as in Eq. (7). The key point to derive the dispersion relation is to analyze acoustic pressure wave propagation in the tubes. As one example, we consider the tube that connects the cuboid compartment at site (m, n) to its Nth nearest neighbor along x-direction at site $(m + N, n)$. The pressure field inside the tube is composed of a forward waveguide mode, from the cuboid at site (m, n) to that at site $(m + N, n)$, and a corresponding backward waveguide mode

$$p(s) = \left(A^+ \exp\left(i\frac{\omega}{v_{\text{air}}}s\right) + A^- \exp\left(-i\frac{\omega}{v_{\text{air}}}s\right)\right)\exp(-i\omega t). \qquad (12)$$

Herein, s indicates the distance along the central axis of the tube, with $s = 0$ corresponding to one end of the tube, where it connects the cuboid at site (m, n). We further have $s = L_N$, with $L_N = d - w + 2h_N + \sqrt{d^2 + N^2 a^2}$ being the tube length, representing the other end. A^+ and A^- are two unknown amplitude coefficients. The corresponding particle velocity is derived as

$$v(s) = \frac{1}{i\omega\rho_0}\frac{\partial p}{\partial s} = \frac{1}{\rho_0 v_{\text{air}}}\left(A^+ \exp\left(i\frac{\omega}{v_{\text{air}}}s\right) - A^- \exp\left(-i\frac{\omega}{v_{\text{air}}}s\right)\right)\exp(-i\omega t), \qquad (13)$$

with ρ_0 representing the average air density as previously. Due to continuity, the acoustic pressure at the two ends of the tube must be the same as in the corresponding cuboids [34]

$$p(0) = \tilde{P}\exp(ik_x ma + ik_y na - i\omega t), \qquad (14)$$

$$p(L_N) = \tilde{P}\exp(ik_x(m + N)a + ik_y na - i\omega t). \qquad (15)$$

The two amplitude coefficients, A^+ and A^-, result from

$$A^+ = \frac{\tilde{P}}{2i}\exp(ik_x ma + ik_y na)\csc\left(\frac{\omega L_N}{v_{\text{air}}}\right)\left(\exp(ik_x Na) - \exp(-i\frac{\omega L_N}{v_{\text{air}}})\right), \qquad (16)$$

$$A^- = \frac{\tilde{P}}{2i}\exp(ik_x ma + ik_y na)\csc\left(\frac{\omega L_N}{v_{\text{air}}}\right)\left(-\exp(ik_x Na) + \exp(i\frac{\omega L_N}{v_{\text{air}}})\right). \qquad (17)$$

Substitution of the above two equations into Eq. (13) leads to the particle velocity

$$v(s) = \frac{i\tilde{P}}{\rho_0 v_{\text{air}}}\csc\left(\frac{\omega L_N}{v_{\text{air}}}\right)\exp(ik_x ma + ik_y na - i\omega t)\left(\cos\left(\frac{\omega s - \omega L_N}{v_{\text{air}}}\right) - \cos\left(\frac{\omega s}{v_{\text{air}}}\right)\exp(ik_x Na)\right). \qquad (18)$$

From this expression, the total air mass flowing away from the cuboid at lattice site (m, n) through the above tube is given by

$$Q_{m+N,n} = \rho_0 S_N v(0) = i\frac{S_N \tilde{P}_{mn}}{v_{\text{air}}}\csc\left(\frac{\omega L_N}{v_{\text{air}}}\right)\left(\cos\left(\frac{\omega L_N}{v_{\text{air}}}\right) - \exp(ik_x Na)\right). \qquad (19)$$

Here, the area $S_N = \pi R_N^2$ represents the cross section of the tube and $v(0)$ the particle velocity at one end of the tube. Similarly, we derive the average mass flow away from the cuboid at lattice site (m, n) through the tube that connects the two cuboids at sites (m, n) and $(m, n + N)$ as

$$Q_{m,n+N} = i\frac{S_N \tilde{P}_{mn}}{v_{\text{air}}}\csc\left(\frac{\omega L_N}{v_{\text{air}}}\right)\left(\cos\left(\frac{\omega L_N}{v_{\text{air}}}\right) - \exp(ik_y Na)\right). \qquad (20)$$

With the conservation law for the air mass inside the cuboid compartment at site (m, n), we have [34]

$$\mathrm{i}\frac{\omega}{v_{\mathrm{air}}^2}V_c\tilde{P}_{mn} = \sum_{N=1}^{\infty}\left(Q_{m+N,n} + Q_{m-N,n} + Q_{m,n+N} + Q_{m,n-N}\right). \tag{21}$$

$Q_{m-N,n}$ is the mass flow through the tube that connects the two cuboids at sites (m, n) and $(m - N, n)$. $Q_{m,n-N}$ is defined analogously. After some mathematical simplifications, we arrive at the following expression for the dispersion relation

$$\frac{\omega}{v_{\mathrm{air}}}V_c = \sum_{N=1}^{\infty}\left(\pi R_N^2 \csc\left(\frac{\omega L_N}{v_{\mathrm{air}}}\right)\left(4\cos\left(\frac{\omega L_N}{v_{\mathrm{air}}}\right) - 2\cos(k_x Na) - 2\cos(k_y Na)\right)\right). \tag{22}$$

V_c represents the volume of the compartment. This equation connects the angular frequency ω with k_x and k_y. For a given Bloch wave vector $\mathbf{k} = (k_x, k_y)$, the implicit formula Eq. (22) provides multiple solutions for ω. These solutions correspond to the different bands. Compared to the previous section, the price we pay for the refined modelling in the present section is that we do not obtain a closed explicit expression for the angular frequency ω as a function of the Bloch wave vector. However, the implicit Eq. (22) can easily be solved numerically. Results are shown by the blue dots in Figs. 3 and 4. They agree well with the numerical FEM calculations (gray curves) regarding the lowest bands as well as the higher bands. For the case of two different orders of long-range interaction in parallel shown in Fig. 5(a)-(c), the qualitative agreement for the lowest bands is again good, but quantitative differences occur, especially along the **MK** direction. The differences are yet more pronounced for the higher bands. We assign these differences to the fact that the vertical parts of the tubes for different N partially overlap (cf. Fig. 2, part with height h_3), leading to interference of the respective partial waves. The refined model neglects these interferences. However, we recall that the focus of this study lies on the lowest bands. For these, the refined model generally performs better than the simple discrete model in Figs. 3-5.

Elastic waves instead of airborne sound. So far, we have exclusively discussed longitudinally polarized airborne sound waves. It is interesting to investigate whether we can translate the overall approach of the metamaterial platform illustrated in Figs. 1 and 2 to elastic waves, for which three modes emerge from the $\boldsymbol{\Gamma}$ point rather than just a single mode for airborne sound. For elastic waves, the structures in Figs. 1 and 2 should be interpreted as being composed of a single ordinary elastic material (e.g., a polymer, see Supplementary Note 3) rather than as air channels. Supplementary Figure 8 provides numerically calculated example band structures for $N = 3,\ 4$, and 5, that can be compared with Fig.4 (a)-(c). Clearly,

the overall behavior of the lowest elastic band is closely similar to that of the lowest band for airborne sound. Specifically, the number of extrema of $\omega(\mathbf{k})$, with $\mathbf{k} = (k, 0)$ or $\mathbf{k} = (0, k)$, versus k in the interval $k \in [0, \pi/a]$ is equal to N – in agreement with the Fourier synthesis idea presented above.

It is presently not clear whether this idea can also be translated to experimentally accessible metamaterial structures for yet other types of waves, such as, e.g., surface water waves, microwaves or light waves. We hope that our work stimulates future experiments and further design studies in this direction.

Data availability

The data that support the plots within this paper and other findings of this study are published on the open access data repository of the Karlsruhe Institute of Technology (https://doi.org/10.35097/565).

Code availability

The numerical simulations in this work for the 2D mass-and-spring model have all been performed by using the commercial software MATLAB. Numerical simulations in this work for the elastic and acoustic metamaterials are all performed using the commercial software COMSOL Multiphysics. The code and models are published on the open access data repository of the Karlsruhe Institute of Technology (https://doi.org/10.35097/565).

Author contributions

K.W. and Y.C. performed all the numerical simulations. Y.C. and M.K. designed the metamaterials. Y.C. and M.W. wrote the first draft. C.W. and M.W. supervised the effort. All authors discussed the results and contributed to the writing and reviewing of the manuscript.

Competing interests

Muamer Kadic is a Guest Editor of *Communications Materials* and was not involved in the editorial review of, or the decision to publish, this Article. All other authors declare no competing interests.

Figures and Captions
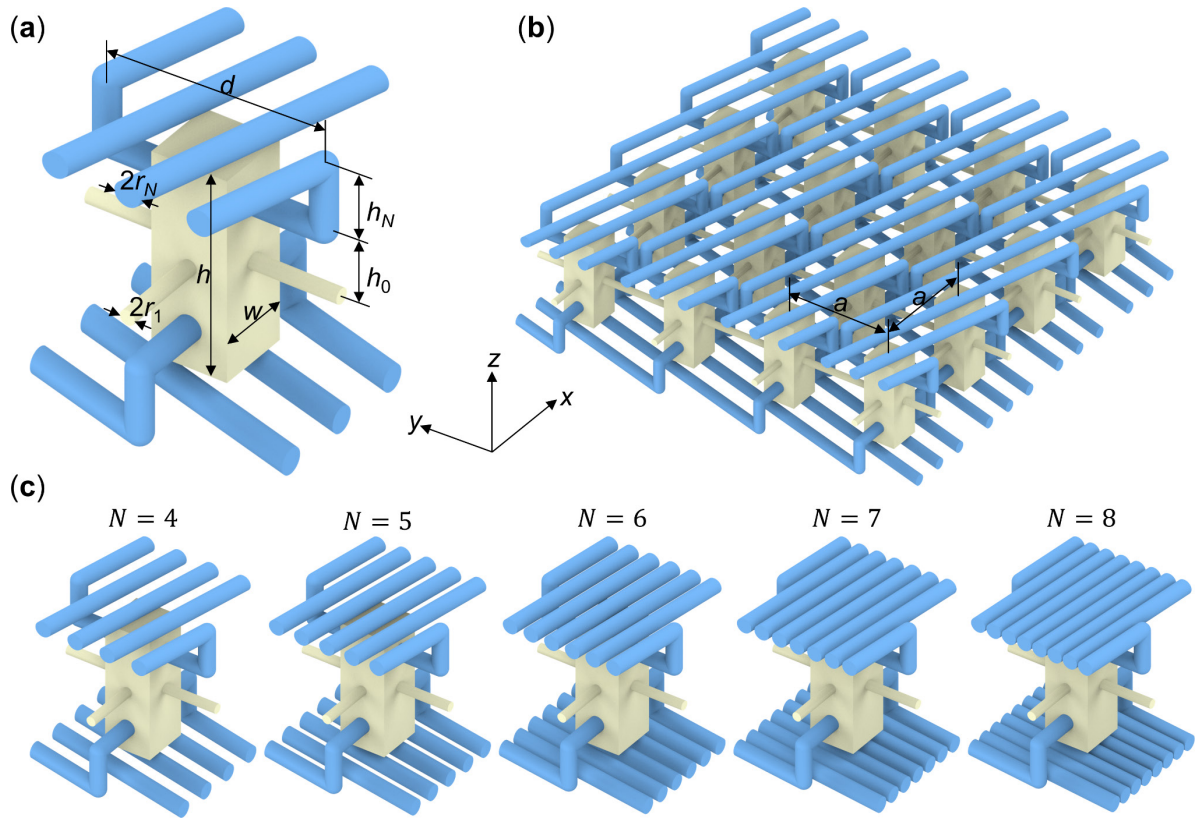
Fig. 1. Considered metamaterial platform supporting beyond-nearest-neighbor interactions along two orthogonal directions. (a) Scheme of a single unit cell for $N = 3$. (b) 2D square lattice with lattice constant a built from this unit cell. The colors are for illustration only. The colored regions form a channel system that is bounded by rigid walls (not shown for clarity). The cuboid compartments (yellow) are connected to their four immediate neighbors along the x- and y-direction by tubes (yellow) with radius r_1. They are further connected to their Nth nearest neighbors by tubes (blue) with radius r_N. The tubes along the x-direction (y-direction) are located above (below) the xy-plane spanned by the yellow tubes. (c) gallery of unit cells for $N = 4$ to $N = 8$ as indicated. For our calculations, we use the following fixed geometrical parameters: $r_1/a = 0.03$, $r_N/a = 0.05$, $w/a = 0.30$, $h/a = 0.80$, $h_0/a = 0.24$, $h_N/a = 0.25$, and $d/a = 0.86$. We choose $a = 10$ cm for the metamaterials supporting airborne sound and $a = 100$ μm for the elastic metamaterials.
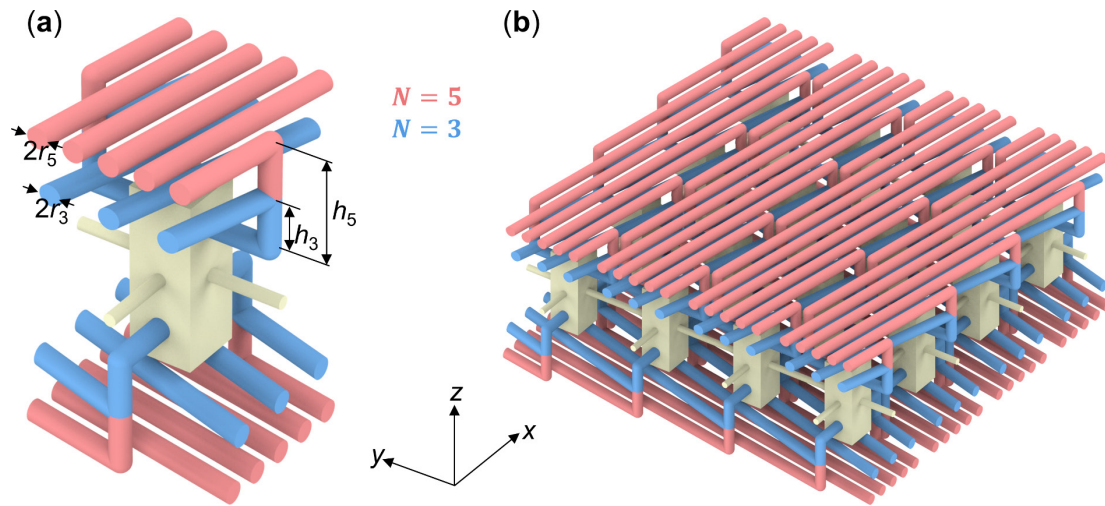
Fig. 2. Same as Fig.1, but tubes (red) mediating the fifth-nearest-neighbor interactions ($N = 5$) are added as an example. (a) Single metamaterial unit cell. (b) 2D square lattice composed thereof. Clearly, yet further values of N could easily be implemented in other planes parallel to the xy-plane at other z-positions below and above the plane spanned by the yellow tubes ($N = 1$). Again, due a rotation-reflection symmetry of the overall structure, wave propagation along the x- and y-direction is equivalent.
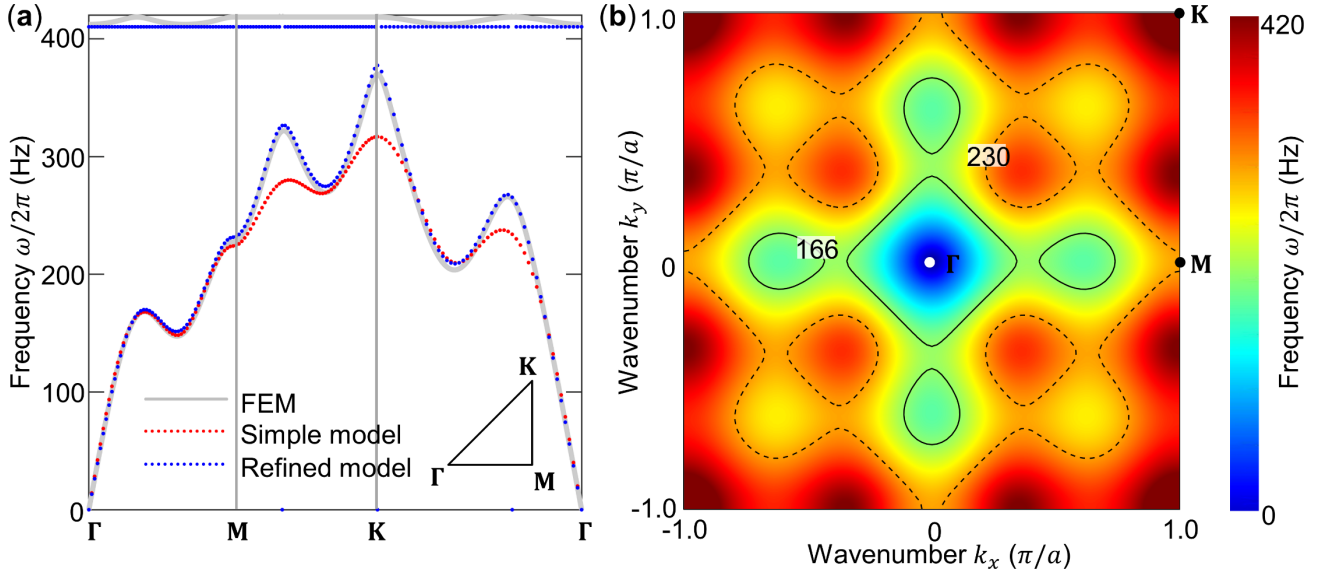
Fig. 3. Calculated phonon dispersion relation for the metamaterial structure shown in Fig. 1, i.e., for $N = 3$ beyond-nearest-neighbor interactions only. (**a**) Tour through the first Brillouin zone (see inset) of the 2D square lattice with lattice constant a. The gray curve is obtained by numerical finite-element-method (FEM) calculations. The analytical results of the simple discrete model are shown by the red curve. Here, only the lowest band occurs. The results of the refined analytical model are shown by the blue dots. These almost completely overlap with the numerical calculations. The agreement with the simple discrete model is qualitatively very good, especially for the principal directions. The parameters for the gray and blue data are given in Fig. 1. The used parameters for the simple discrete model are: $M = \rho V_c = 9.3 \times 10^{-5}$ g, $K_1 = 27.9$ N m^{-1}, and $K_3 = 17.7$ N m^{-1}. (**b**) Frequency as obtained from the numerical finite-element calculations represented on a false-color scale versus wavenumber k_x and k_y within the first Brillouin zone of the square lattice.
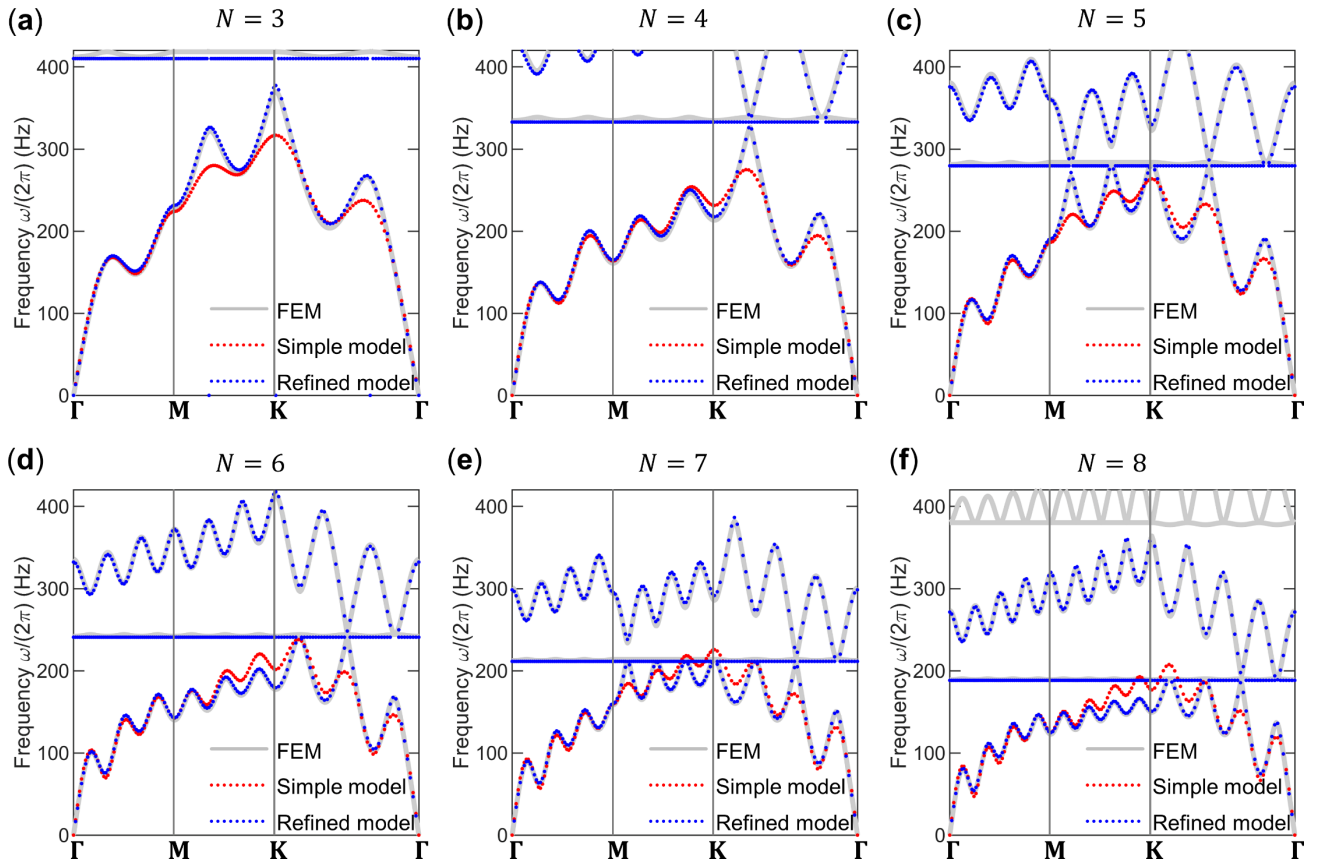
Fig. 4. Dispersion relations as in Fig. 3(a), but for different orders N of beyond-nearest-neighbor interactions in addition to the nearest-neighbor interactions. (**a**) $N = 3$. (**b**) $N = 4$. (**c**) $N = 5$. (**d**) $N = 6$. (**e**) $N = 7$. (**f**) $N = 8$. The corresponding metamaterial structures are depicted in Fig. 1(c).
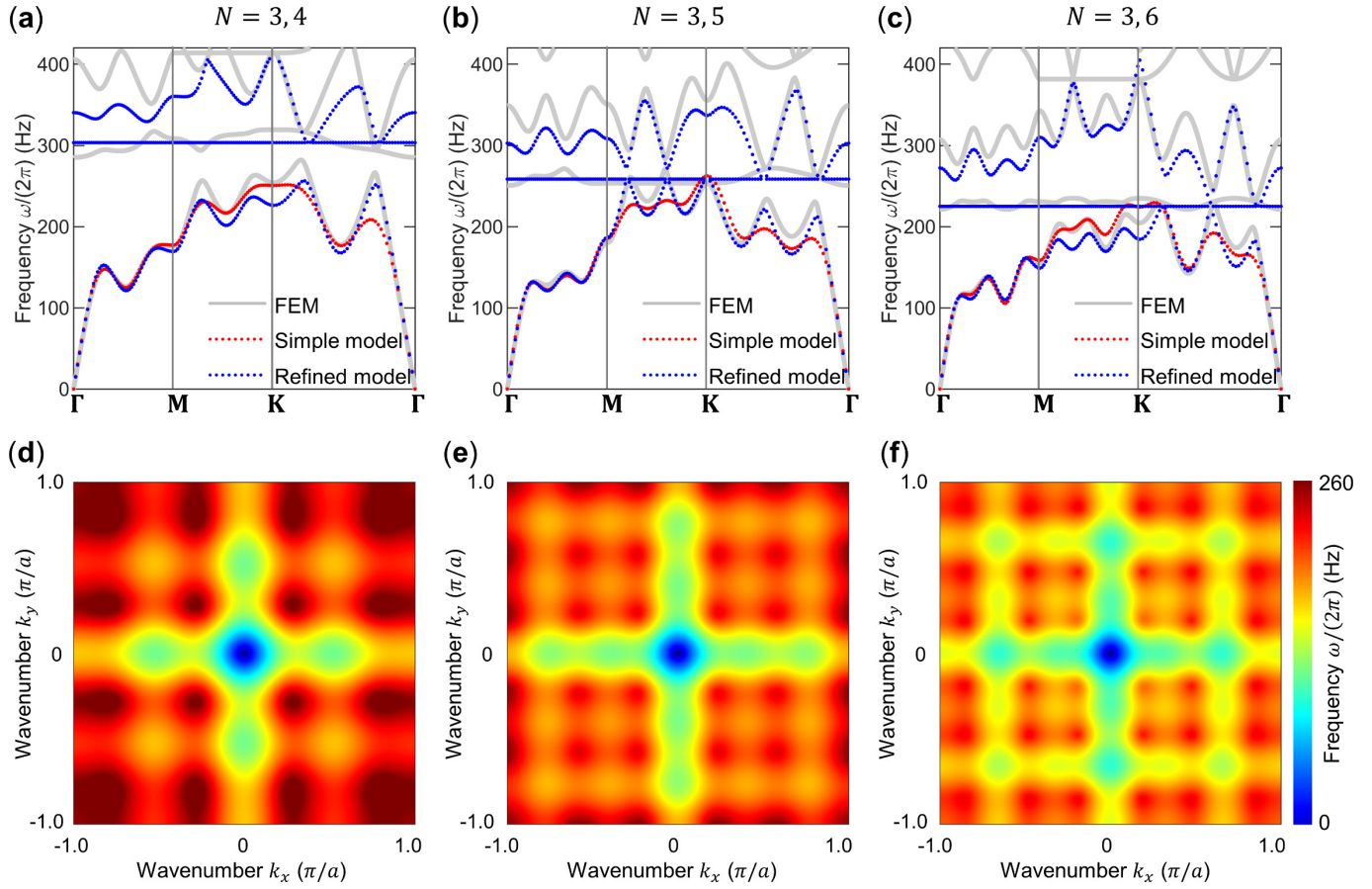
Fig. 5. Calculated phonon dispersion relations for metamaterial structures as shown in Fig. 2. Compared to the dispersion relations shown in Fig. 3, two different beyond-nearest-neighbor interactions are present simultaneously here. (**a**) - (**c**) correspond to $N = 3$ and $N = 4$ simultaneously, $N = 3$ and $N = 5$ simultaneously, and $N = 3$ and $N = 6$ simultaneously, respectively. Results from the numerical calculations (gray), the simple discrete model (red), and the refined analytical model (blue) are compared. (**d**) - (**f**) False-color representations of frequency versus wavenumber k_x and k_y from the numerical calculations. The behavior is due to the combined action of two different beyond-nearest-neighbor interactions.
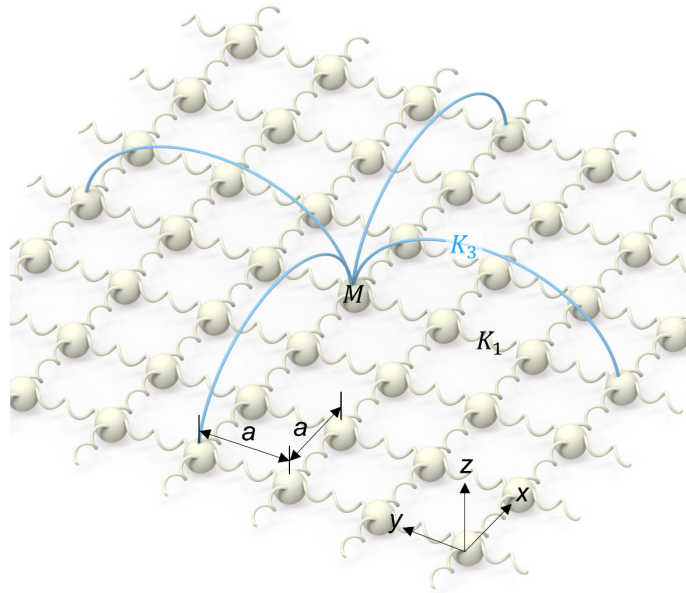
Fig. 6. The shown 2D mass-and-spring model is mathematically equivalent to an approximate discrete model of the 2D metamaterial lattice shown in Fig. 1(b). To allow for comparison, the color of the masses (yellow) corresponds to that of the cuboid compartments in Fig. 1(b). Likewise, the nearest-neighbor Hooke's springs (yellow) correspond to the nearest-neighbor tubes in Fig. 1(b). The beyond-nearest-neighbor Hooke's springs with spring constants K_N, exemplified here for the case of $N = 3$, are schematically illustrated by the blue lines. For clarity, they are only depicted for a single mass in the lattice. All masses M in the square lattice with lattice constant a are identical. Analytical dispersion relations obtained from this model are shown by the red dots in Figs. 3 and 4 (also see Supplementary Figure 4). By virtue of the good agreement to the complete numerical calculations, the simple discrete model allows for discussing the highly unusual wave behavior at interfaces with reasonable effort (see Figs. 8-10).
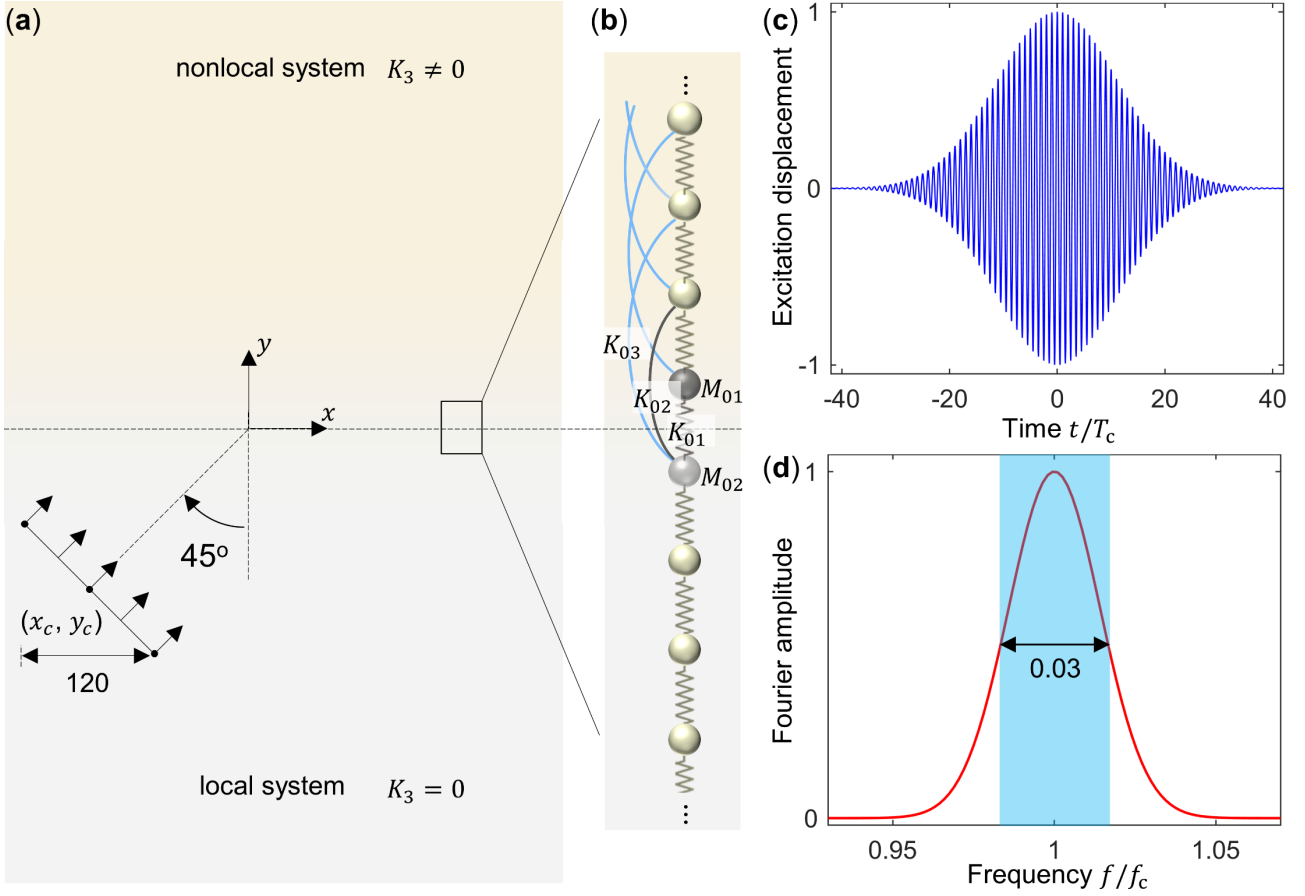
Fig. 7. Simulation setup of wave refraction at interface. (**a**) Wave transmission at an interface between a local system with only nearest-neighbor interactions (bottom, gray) and a nonlocal system additionally including third-nearest-neighbor interactions, $K_3 \neq 0$ (top, yellow). The incident wave impinges under an angle of $45°$ onto the interface. (**b**) Due to the mismatch of interaction orders between the two regions, some of the third-order Hooke's springs are cut away near the interface (dashed horizontal line) within the nonlocal region. To control the transmission of the incident waves, we fine-tune the mass parameters, M_{01} and M_{02}, and three Hooke's spring constants, K_{01}, K_{02}, and K_{03}, at the interface. To avoid reflection of the partial waves at the boundaries of the simulation domain, we choose a much larger simulation domain than the one shown. A wave packet that is Gaussian in space and time is launched by prescribing the pressure in Eq. (4) on the black lines according to $\cos(2\pi f_c t)\exp(-(\pi f_c t/50)^2)\exp(-((x-x_c)^2 + (y-y_c)^2)/37.5^2)$. (**c**) Temporal profile of the launched pulse, containing about 50 oscillation cycles. (**d**) Corresponding Fourier transform (absolute value).
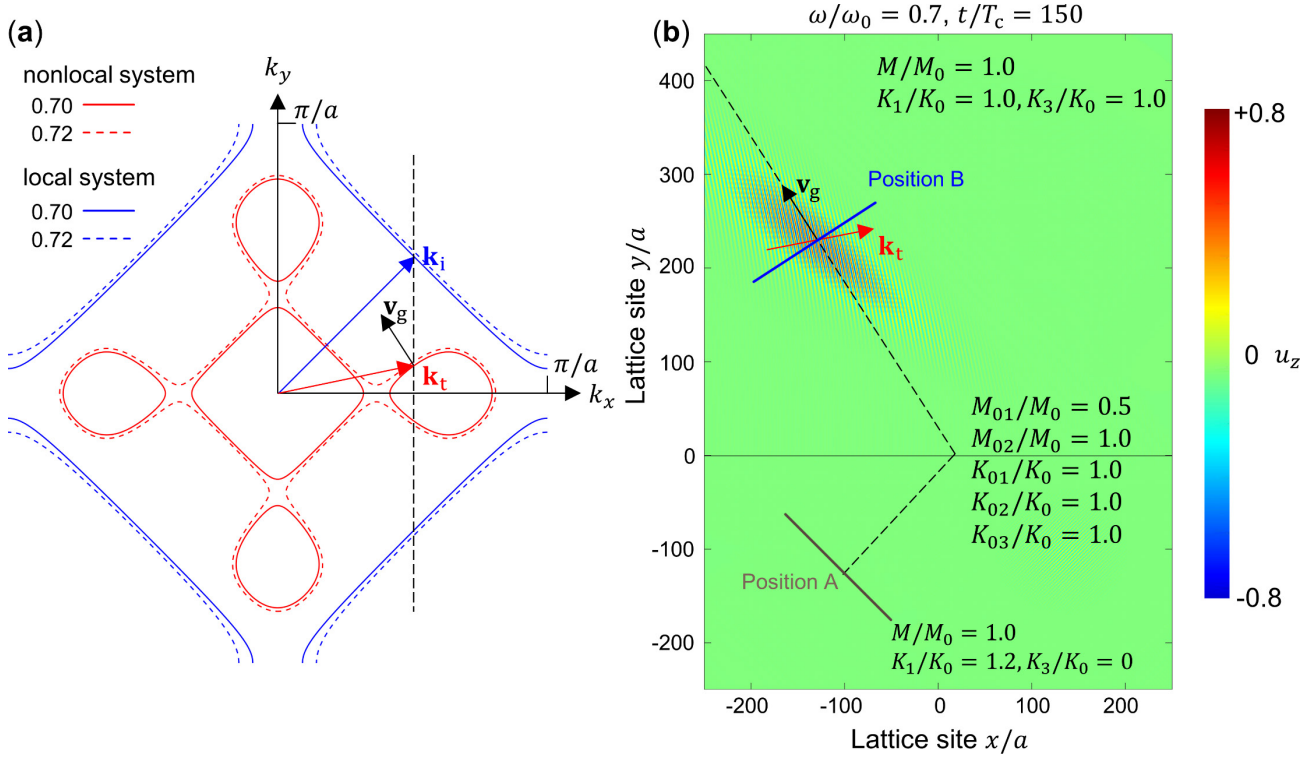
Fig. 8. Negative refraction at an interface as illustrated in Fig. 7. (**a**) Iso-frequency curves for the nonlocal system, with the same parameters as in Supplementary Figure 4, and the local system, with parameters $M/M_0 = 1$, $K_1/K_0 = 1.2$, and $K_3/K_0 = 0$. The solid lines correspond to the carrier frequency $\omega_c/\omega_0 = 0.7$ of the Gaussian pulse. The blue arrow represents the incident wave vector, $\mathbf{k}_i$. From Snell's law, a single negatively refracted mode with wave vector, $\mathbf{k}_t$, and group velocity vector, $\mathbf{v}_g$, is possible. (**b**) Snapshot of simulated pressure fields at $t/t_c = 150$, with $t_c = 2\pi/\omega_c$. The interface parameters (cf. Fig. 7) are $M_{01}/M_0 = 0.5$, $M_{02}/M_0 = 1.0$, $K_{01}/K_0 = 1.0$, $K_{02}/K_0 = 1.0$, and $K_{03}/K_0 = 1.0$. The black dashed straight lines indicate the propagation path of the incident and the refracted wave. In the nonlocal region, the wave propagation direction agrees well with the group velocity vector as derived in panel (**a**). An animated version of (**b**) is provided in the Supplementary Movie 1. The displacement component u_z for the two cuts perpendicular to the propagation direction at positions A (brown) and B (blue), respectively, is shown in Supplementary Figure 5.
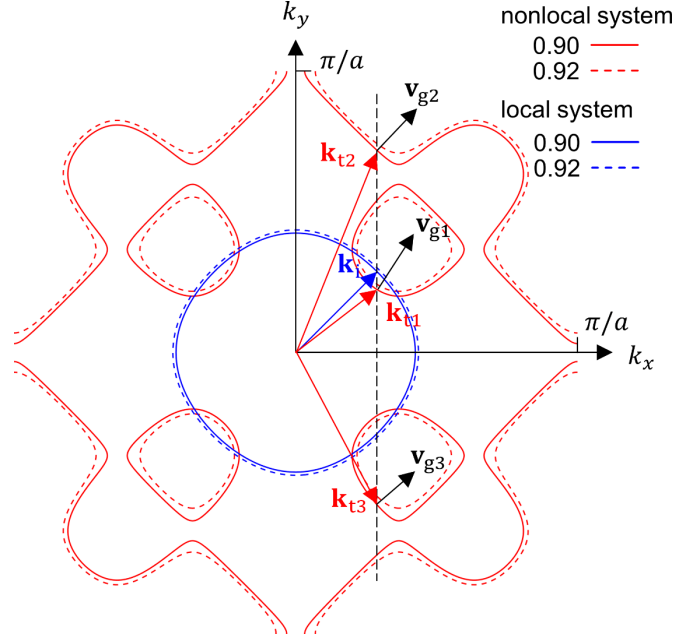
Fig. 9. Triple refraction at an interface as illustrated in Fig. 7. Iso-frequency contours for the nonlocal system, with the same parameters as in Supplementary Figure 4, and the local system, with parameters $M/M_0 = 0.44$, $K_1/K_0 = 2.3$, and $K_3/K_0 = 0$. The solid lines correspond to the carrier frequency $\omega_c/\omega_0 = 0.9$ of the excited Gaussian wave packet. By using Snell's law, triple refraction with wave vectors, $\mathbf{k}_{t1}$, $\mathbf{k}_{t2}$ and $\mathbf{k}_{t3}$, and corresponding group velocity vectors, $\mathbf{v}_{g1}$, $\mathbf{v}_{g2}$ and $\mathbf{v}_{g3}$, becomes possible. The partial wave with wave vector $\mathbf{k}_{t3}$ and group velocity vector $\mathbf{v}_{g3}$ is a backward wave with $\mathbf{k}_{t3} \cdot \mathbf{v}_{g3} < 0$.
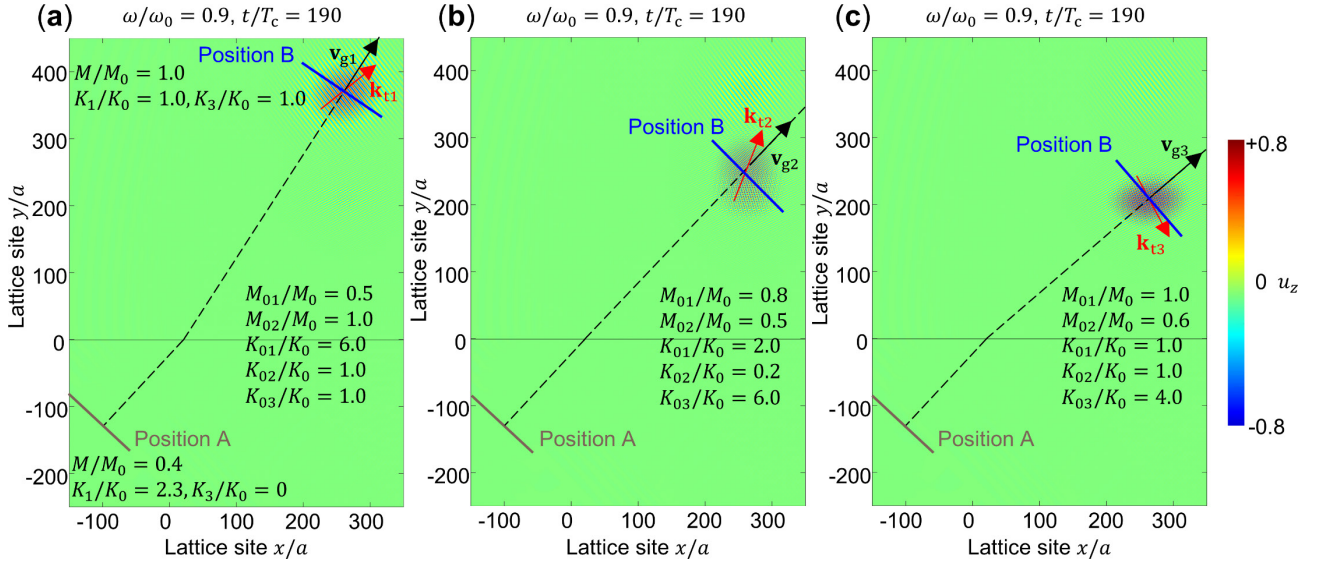
Fig. 10. Relative amplitude control of the three refracted modes at the interface between a nonlocal system and a local system by tuning the interface parameters illustrated in Fig. 7(b). (a) Snapshot of simulated pressure fields with the interface parameters, $M_{01}/M_0 = 0.5$, $M_{02}/M_0 = 1.0$, $K_{01}/K_0 = 6.0$, $K_{02}/K_0 = 1.0$, and $K_{03}/K_0 = 1.0$, respectively. In this case, only the refracted mode with the wave vector $\mathbf{k}_{t1}$ and group velocity vector $\mathbf{v}_{g1}$ occurs. The dashed lines indicate the propagation path of the incident and refracted waves. (b), (c) Same as (a), but with interface parameters $M_{01}/M_0 = 0.8$, $M_{02}/M_0 = 0.5$, $K_{01}/K_0 = 2.0$, $K_{02}/K_0 = 0.2$, $K_{03}/K_0 = 6.0$, and $M_{01}/M_0 = 1.0$, $M_{02}/M_0 = 0.6$, $K_{01}/K_0 = 1.0$, $K_{02}/K_0 = 1.0$, and $K_{03}/K_0 = 4.0$, respectively. Animated versions of the three scenarios are provided in the Supplementary Movies 2-4. The displacement component u_z for the cuts perpendicular to the propagation direction at the positions A (brown) and B (blue) in panels (a)-(c) is shown in Supplementary Figure 6.

References

[1]   C. Kittel, *Introduction to solid state physics*. (Wiley, New York, 2005).

[2]   R. Hoppe, Madelung constants, Angewandte Chemie International Edition in English **5**, 1 (1966).

[3]   Z. Liu, X. Zhang, Y. Mao, Y. Zhu, Z. Yang, C. T. Chan and P. Sheng, Locally resonant sonic materials, Science **289**, 5485 (2000).

[4]   D. R. Smith, J. B. Pendry and M. Wiltshire, Metamaterials and negative refractive index, Science **305**, 5685 (2004).

[5]   W. Cai and V. M. Shalaev, *Optical metamaterials*. (Springer, New York, 2010).

[6]   M. Decker, N. Feth, C. M. Soukoulis, S. Linden and M. Wegener, Retarded long-range interaction in split-ring-resonator square arrays, Phys. Rev. B **84**, 8 (2011).

[7]   M. Decker, S. Burger, S. Linden and M. Wegener, Magnetization waves in split-ring-resonator arrays: Evidence for retardation effects, Phys. Rev. B **80**, 19 (2009).

[8]   Y. Liu, X. Su and C. T. Sun, Broadband elastic metamaterial with single negativity by mimicking lattice systems, J. Mech. Phys. Solids **74**, 158 (2015).

[9]   Y. Chen, X. Liu and G. Hu, Topological phase transition in mechanical honeycomb lattice, J. Mech. Phys. Solids **122**, 54 (2019).

[10]   H. Zhang, Y. Chen, X. Liu and G. Hu, An asymmetric elastic metamaterial model for elastic wave cloaking, J. Mech. Phys. Solids **135**, 103796 (2020).

[11]   H. Chen, H. Nassar and G. L. Huang, A study of topological effects in 1D and 2D mechanical lattices, J. Mech. Phys. Solids **117**, 22 (2018).

[12]   D. Gazis, R. Herman and R. Wallis, Surface elastic waves in cubic crystals, Phys. Rev. **119,** 14 (1960).

[13]   J. Tersoff, Empirical interatomic potential for silicon with improved elastic properties, Phys. Rev. B **38**, 2 (1988).

[14]   S. A. Cummer, J. Christensen and A. Alù, Controlling sound with acoustic metamaterials, Nat. Rev. Mater. **1**, 3 (2016).

[15]   K. Bertoldi, V. Vitelli, J. Christensen and M. Van Hecke, Flexible mechanical metamaterials, Nat. Rev. Mat. **2**, 11 (2017).

[16]   H. Dong, S. Zhao, Y. Wang and C. Zhang, Topology optimization of anisotropic broadband double-negative elastic metamaterials, J. Mech. Phys. Solids **105**, 54 (2017).

[17]   M. Kadic, G. W. Milton, M. van Hecke and M. Wegener, 3D metamaterials, Nat. Rev. Phys. **1**, 3 (2019).

[18]   G. Cottone, M. Di Paola and M. Zingales, Elastic waves propagation in 1D fractional non-local continuum, Physica E **42**, 2 (2009).

[19]   A. Carpinteri, P. Cornetti and A. Sapora, Nonlocal elasticity: an approach based on fractional calculus, Meccanica **49**, 11 (2014).

[20]   M. Di Paola and M. Zingales, Long-range cohesive interactions of non-local continuum faced by fractional calculus, Int. J. Solids Struct. **45**, 21 (2008).

[21]   H. Cho, J. C. Weaver, E. Pöselt, P. J. in't Veld, M. C. Boyce and G. C. Rutledge, Engineering the mechanics of heterogeneous soft crystals, Adv. Funct. Mater. **26**, 38 (2016).

[22]   L. Frieder and M. J. Vellekoop, Bandgap engineering of three-dimensional phononic crystals in a simple cubic lattice, Appl. Phys. Lett. **113**, 20 (2018).

[23]   L. Daniel, S. Mittal, M. Hafezi and Y. D. Chong, Reconfigurable topological phases in next-nearest-neighbor coupled resonator lattices, Phys. Rev. **121**, 2 (2018).

[24]   Y. Chen, M. Kadic and M. Wegener, Roton-like acoustical dispersion relations in 3D metamaterials, Nat. Commun. **12**, 1 (2021).

[25]   J. A. I. Martínez, M. F. Groß, Y. Chen, T. Frenzel, V. Laude, M. Kadic and M. Wegener, Experimental Observation of Roton-Like Dispersion Relations in Metamaterials, Sci. Adv. **7**, eabm2189 (2021).

[26]   L. Landau, Theory of the Superfluidity of Helium II, Phys. Rev. **60**, 4 (1941).

[27]   R. P. Feynman, Atomic theory of the two-fluid model of liquid helium, Phys. Rev. **94**, 2 (1954).

[28]   R. P. Feynman and M. Cohen, Energy spectrum of the excitations in liquid helium, Phys. Rev. **102**, 5 (1956).

[29]   H. Godfrin, K. Beauvois, A. Sultan, E. Krotscheck, J. Dawidowski, B. Fåk and J. Ollivier, Dispersion relation of Landau elementary excitations and thermodynamic properties of superfluid He 4, Phys. Rev. B **103**, 10 (2021).

[30]   R. Fleury, Non-local oddities, Nat. Phys. **17**, 766 (2021).

[31]   V. Peri, Z. Song, M. Serra-Garcia, P. Engeler, R. Queiroz, X. Huang, W. Deng, Z. Liu, B. A. Bernevig and S. D. Huber, Experimental characterization of fragile topology in an acoustic metamaterial, Science **367**, 6479 (2020).

[32]   R. Zhu, X. Liu, G. Hu, C. T. Sun and G. Huang, Negative refraction of elastic waves at the deep-subwavelength scale in a single-phase metamaterial, Nat. Commun. **5**, 5510 (2014).

[33]   X. Liu, G. Hu, G. Huang and C. Sun, An elastic metamaterial with simultaneously negative mass density and bulk modulus, Appl. Phys. Lett. **98**, 251907 (2011).

[34]   A. D. Pierce, *Acoustics: an introduction to its physical principles and applications*. (Springer, New

York, 2019).

[35]   D. J. Griffiths, *Introduction to electrodynamics*. (Cambridge University Press, London, 2017).

[36]   T. Frenzel, J. D. Brehm, T. Bückmann, R. Schittny, M. Kadic and M. Wegener, Three-dimensional labyrinthine acoustic metamaterials, Appl. Phys. Lett. **103**, 6 (2013).

From nonlocal oddities to roton-like dispersion relations and beyond

– Supplementary Materials

Ke Wang[1,2]†, Yi Chen[1]†*, Muamer Kadic[1,3], Changguo Wang[2], Martin Wegener[1,4]

[1]Institute of Applied Physics, Karlsruhe Institute of Technology (KIT), Karlsruhe 76128, Germany.

[2]Center for Composite Materials, Harbin Institute of Technology, Harbin 150001, P.R. China.

[3]Institut FEMTO-ST, UMR 6174, CNRS, Université de Bourgogne Franche-Comté, Besançon 25030, France.

[4]Institute of Nanotechnology, Karlsruhe Institute of Technology (KIT), Karlsruhe 76128, Germany.

*Correspondence to: yi.chen@partner.kit.edu

†These authors contributed equally.

Supplementary Note 1: Impact of damping effect. Supplementary Figure 1 exhibits the numerically calculated phonon dispersion relations for the metamaterial structure as in Fig. 3 (no damping), but accounting for damping. Panels (a) and (b) show the real and imaginary part of the eigenfrequencies, respectively. For comparison, results without damping are reproduced by the gray solid lines. In the numerical simulations, we include damping through the setting of "narrow region acoustics" in COMSOL Multiphysics. As for the case of zero damping, we employ the usual Bloch periodic boundary conditions. This choice leads to purely real-valued wave vectors. The material parameters chosen for air are: heat capacity $C_\mathrm{p} = 1.01 \times 10^3 \, \mathrm{J \, kg^{-1} \, K^{-1}}$, thermal conductivity $\kappa = 2.57 \times 10^{-2} \, \mathrm{W \, m^{-1} \, K^{-1}}$, ratio of specific heats $\gamma = 1.4$, and dynamic viscosity $\eta = 1.81 \times 10^{-5} \, \mathrm{Pa \cdot s}$, respectively. The mass density and the speed of sound for air are the same as in the main text. The real part of the eigenfrequencies changes by less than 4% when considering damping. The imaginary part is nearly two orders of magnitude smaller than the real part. Most importantly, the overall qualitative behavior is not changed in the presence of damping and roton-like dispersion relations are still obtained. An example for a frequency contour plot versus wave numbers k_x and k_y is shown in Supplementary Figure 2. The real part in panel (b) can be directly compared with Fig. 3(b). These calculations justify the assumption of zero damping that we use throughout the entire main paper.
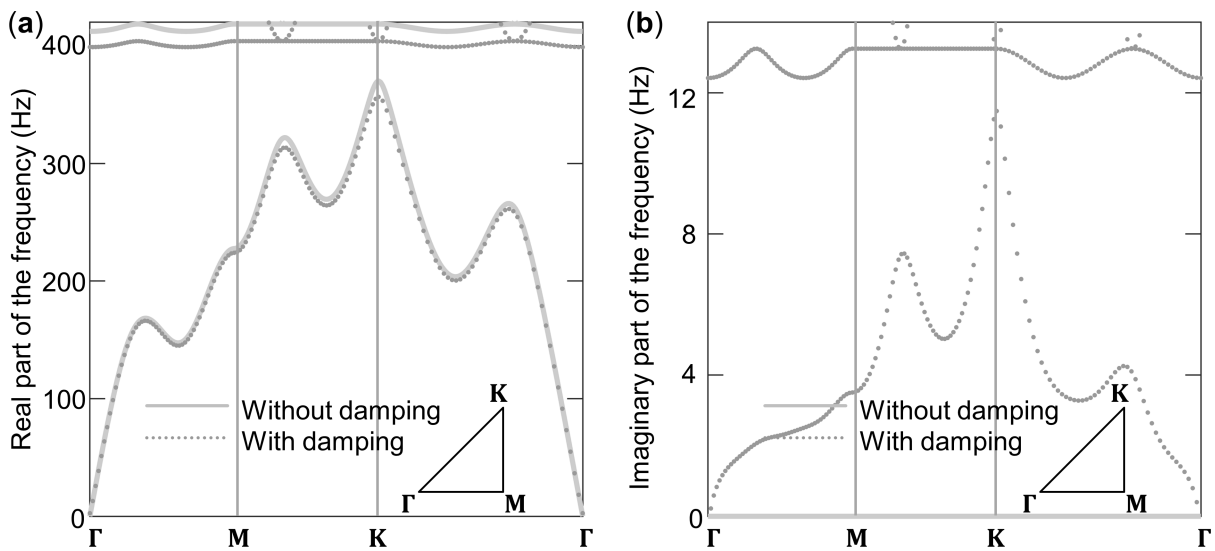
Supplementary Figure 1. Comparison between numerically calculated phonon dispersion relations for the metamaterial as in Figure 3 without damping and with damping. (a) Real and (b) imaginary part of the calculated eigenfrequencies, respectively. The solid gray curves refer to zero damping, the dotted curves to finite damping. Note that the imaginary part in panel (b) is nearly two orders of magnitude smaller than the real part in panel (a).
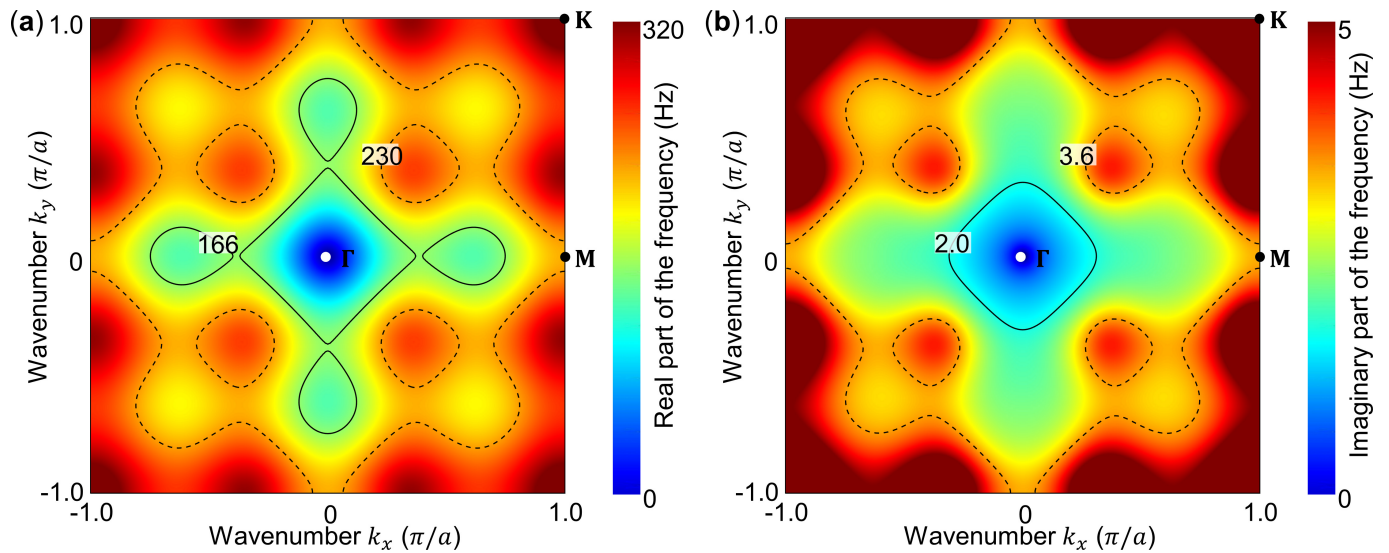
Supplementary Figure 2. **2D Frequency contour plots versus the wavenumbers k_x and k_y for the metamaterial as in Figure 3, but accounting for damping.** (a) Real part. The frequency contour is in very good qualitative agreement with the results shown in Fig. 3(b) for zero damping. (b) Imaginary part. Be aware of the two different false-color scales.
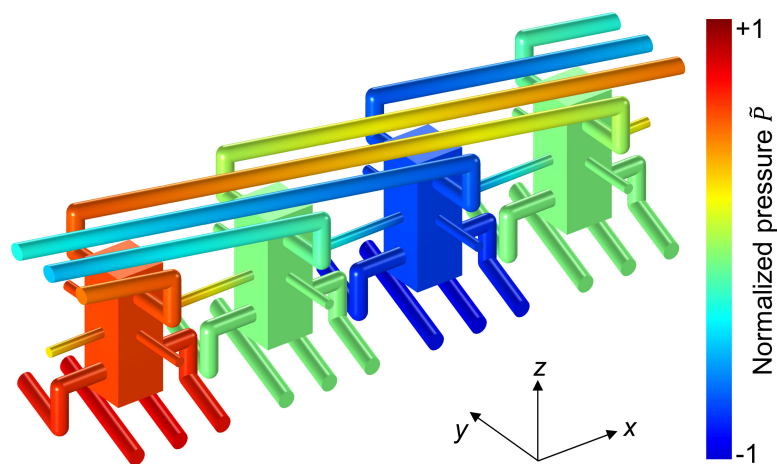

Supplementary Figure 3. False-color representation of the acoustic pressure field (normalized) of the Bloch eigenstate for the metamaterial structure shown in Fig. 1 corresponding to a wave vector $k = (0.5\,\pi/a,\ 0)$. For clarity, an array of 4×1 unit cells is depicted. It can be seen that the pressure is nearly constant within the compartments but exhibits a gradient along the axes of the tubes. This gradient can be interpreted in terms of an effective force, hence in terms of a Hooke's spring constant of the tube.

Supplementary Note 2: Simple discrete model (mass-and-spring model). Supplementary Figure 4 shows an exemplary analytically calculated dispersion relation of the 2D simple discrete model according to Eq. (8). The chosen parameters are given in the figure caption. In panel (b), we have highlighted selected iso-frequency contours to ease the discussion in the main text.
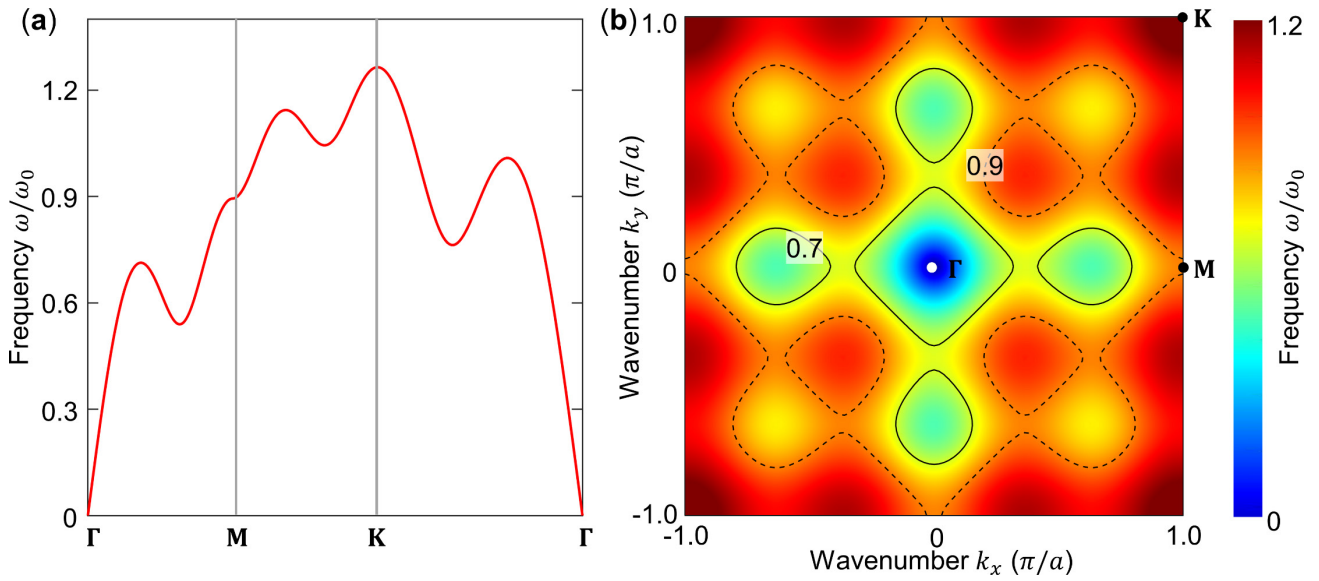
Supplementary Figure 4. Example dispersion relation of the 2D mass-and-spring system in Fig. 6. Here, we only include nearest-neighbor interactions and third-nearest-neighbor interactions (cf. Fig. 3). (**a**) Dispersion relation for the usual tour through the first Brillouin zone of the square lattice. Roton-like minima occur along both, the $\mathbf{\Gamma M}$ and the $\mathbf{\Gamma K}$ direction. (**b**) 2D Frequency contour plot, ω/ω_0, versus the wavenumbers k_x and k_y. We choose the parameters $M/M_0 = 1.0$ and $K_1/K_0 = K_3/K_0 = 1.0$. The reference frequency is $\omega_0 = \sqrt{10K_0/M_0}$. This reference frequency is also used in the calculations shown in Figs. 8-10.
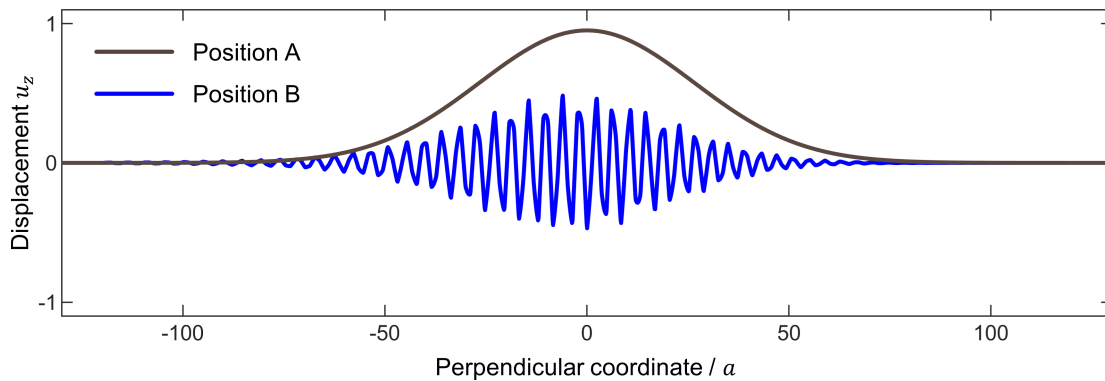
Supplementary Figure 5. Calculated displacement (normalized) versus perpendicular coordinate at the marked positions A and B for the negative refraction in Fig. 8. The displacement for position A is extracted at $t/T_c = 0$ while for position B is $t/T_c = 150$.
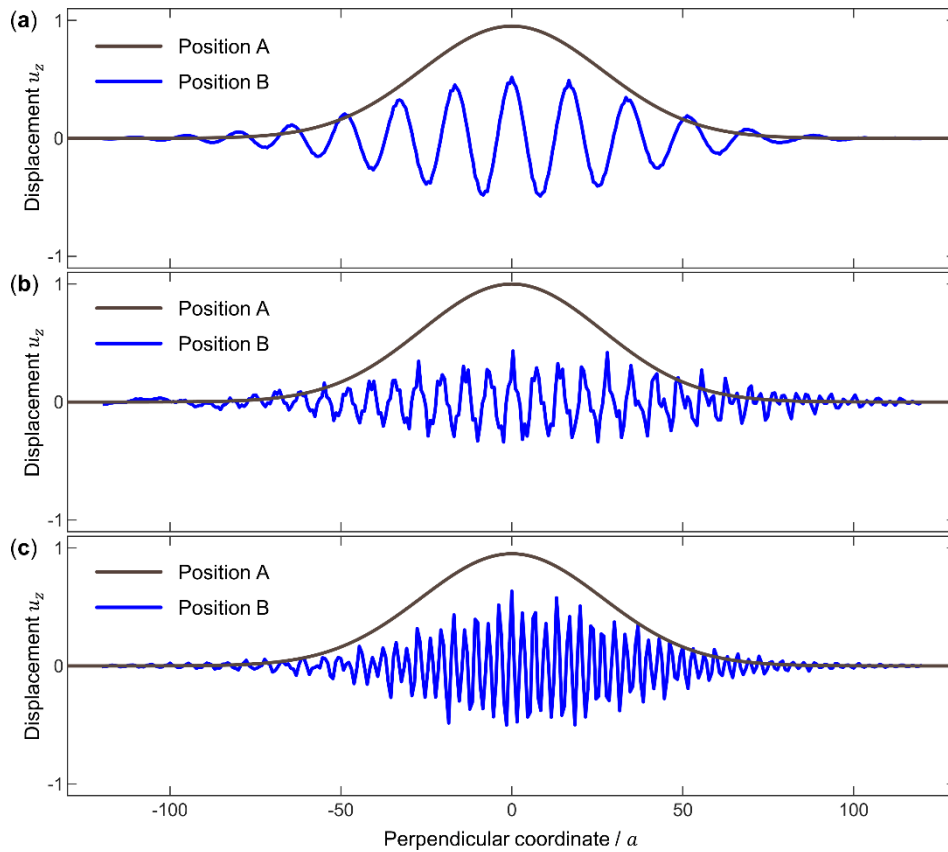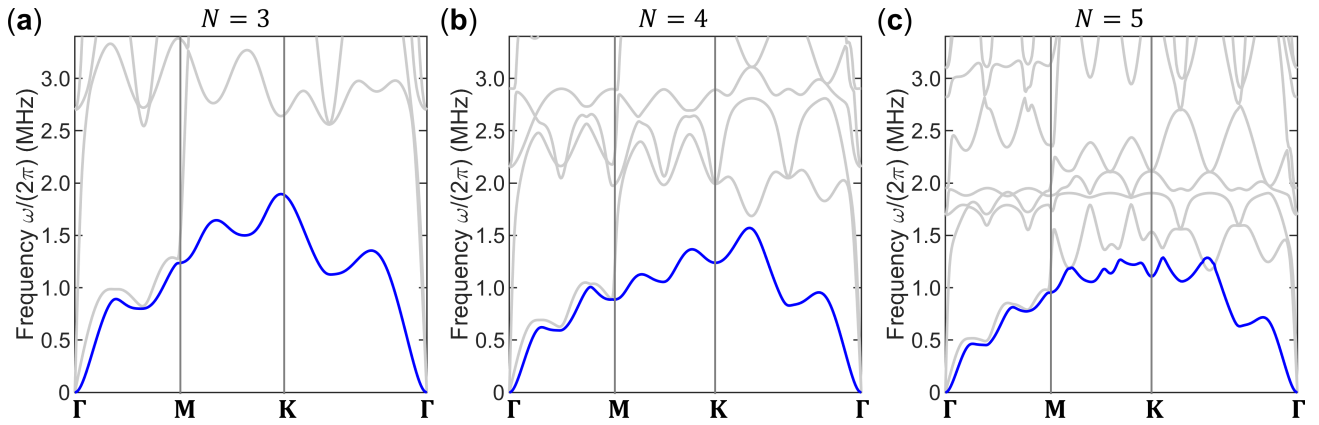
Supplementary Figure 6. Similar to Supplementary Figure 6 but for the triple refractions demonstrated in Fig. 10. (a) (b) (c) Cross-sectional displacement profile plots correspond to 10 (a), (b), and (c), respectively. The displacement for position A is extracted at $t/T_c = 0$, that for position B at $t/T_c = 190$.
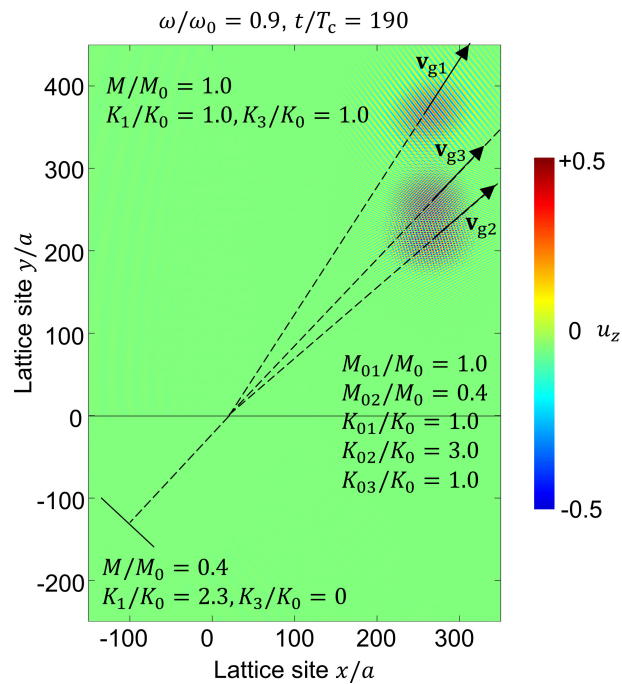
Supplementary Figure 7. As Fig. 10, but with a different set of interface parameters for exciting three refracted modes simultaneously. The interface parameters are indicated in the figure.

Supplementary Note 3: Metamaterials for elastic waves rather than airborne sound. We investigate whether the metamaterial platform including beyond-nearest-neighbor interactions along two orthogonal directions suggested in Fig. 1 for airborne (longitudinal) pressure waves can also serve to realize corresponding elastic metamaterials. In this case, all rods and cuboids are massive (rather than hollow) and made from only a single constituent material. We choose typical polymer parameters with $E = 4.19\,\text{GPa}$ for the Young's modulus, $\nu = 0.4$ for the Poisson's ratio, and $\rho = 1140\,\text{kg m}^{-3}$ for the mass density [1]. Floquet-Bloch periodic boundary conditions are applied to the four sides of the unit cell shown in Fig. 1, while all other boundaries are treated as stress free. We solve the band structure by using the built-in Solid Mechanics Module in COMSOL Multiphysics. The geometry is meshed with around 80 thousand tetrahedral to ensure convergence.

In Supplementary Figure 8 (a)-(c), we plot the calculated phonon band structure for the example of third-nearest-neighbor $(N = 3)$, forth-nearest-neighbor $(N = 4)$, and fifth-nearest-neighbor $(N = 5)$ interactions, respectively. In order to increase the beyond-nearest-neighbor interactions, we choose slightly different rod diameters than above here, i.e., $r_1/a = 0.02$ and $r_N/a = 0.06$. With the latter, we can obtain a maximum of $N = 6$, i.e., for $N \geq 7$ the rods overlap. For the plate-like 2D metamaterial structure, as expected, three bands originate from the $\mathbf{\Gamma}$ point. The one starting quadratically from the $\mathbf{\Gamma}$ point (marked in blue) corresponds to an out-of-plane flexure wave. This mode is similar to an out-of-plane vibration. We find minima in the dispersion relation along both, the $\mathbf{\Gamma M}$ and the $\mathbf{\Gamma K}$ directions. As for the case of airborne sound waves (cf. Fig. 4), the number of oscillations on this band increases with increasing N. This behavior is in agreement with the discussion on the mass-and-spring model in section 3. The other two modes start linearly at the $\mathbf{\Gamma}$ point. The one with larger (smaller) phase velocity is an in-plane longitudinal (shear) wave. The shear band exhibits roton-like minima of the dispersion relation along multiple directions, while the longitudinal band strongly interacts with higher bands, leading to a more complicated behavior.

(a) $N = 3$ **(b)** $N = 4$ **(c)** $N = 5$

Supplementary Figure 8. Phonon dispersion relation for the same geometry as shown in Fig. 1, but for an elastic metamaterial instead of an acoustical metamaterial. The colors in Fig. 1 are for illustration only; the cuboids and cylinders are made from the same constitutive elastic material. (a) − (c) Phonon band structures for the cases $N = 3,\ 4$, and 5, respectively. The lowest (flexural) band is highlighted in blue, all other bands are gray. The cylinder radii are $r_1/a = 0.02$ and $r_N/a = 0.06$, respectively. All other parameters are the same as in Fig. 1. For the constituent material, we choose $E = 4.19\,\mathrm{GPa}$ for the Young's modulus, $\nu = 0.4$ for the Poisson's ratio, and $\rho = 1140\,\mathrm{kg\,m^{-3}}$ for the mass density. These parameters correspond to a typical polymer amenable to 3D laser micro-printing.

Supplementary References

[1]   T. Frenzel, M. Kadic and M. Wegener, Three-dimensional mechanical metamaterials with a twist, Science **358**, 6366 (2017).